




Microstructural modelling of creep crack growth from

metadata, citation and similar papers at core.ac.uk

brought to you by  CORE

provided by University of Groningen Digital Archive

P.R. ONCK and E. VAN DER GIESSEN

Delft University of Technology, Koiter Institute Delft, Mekelweg 2, 2628 CD Delft, The Netherlands;
e-mail: e.vandergiesen@wbmt.tudelft.nl

Received 4 February 1998; accepted in revised form 11 August 1998

Abstract. The effect of crack tip blunting on the initial stages of creep crack growth is investigated by means of a planar microstructural model in which grains are represented discretely. The actual linking-up process of discrete microcracks with the macroscopic crack is simulated, with full account of the underlying physical mechanisms such as the nucleation, growth and coalescence of grain boundary cavities accompanied by grain boundary sliding. Results are presented for C^* -controlled mode I crack growth under small-scale damage conditions. Particular attention is focused on creep constrained vs. unconstrained growth. Also the effect of grain boundary shear stresses on linking-up is investigated through shear-modified nucleation and growth models. The computations show a general trend that while an initially sharp crack tends to propagate away from the original crack plane, crack tip blunting reduces the crack growth direction. Under unconstrained conditions this can be partly rationalized by the strain rate and facet stress distribution corresponding to steady-state creep.

Key words: Creep, cavitation, intergranular fracture, micromechanics.

1. Introduction

The prediction of design life and remaining lifetime of components in high-temperature applications is often based on fracture mechanics techniques using appropriate similitude load parameters such as C^* . This allows for the transfer of crack growth rates from test specimens to components in service, without addressing the actual near-tip failure mechanisms that are responsible for fracture. However, from scientific and material-design points of view, it is interesting to know how these physical mechanisms and their interaction with the crack tip fields affects the crack growth behaviour.

Creep failure in polycrystalline materials starts with the nucleation of cavities on the grain boundary facets. These cavities nucleate and grow under typical high-temperature mechanisms like diffusion, dislocation creep and grain boundary sliding until they coalesce and form facet-sized microcracks. The final intergranular fracture occurs when those microcracks link-up with the macroscopic crack. The above mechanisms have been well established and several overviews have appeared in the literature (e.g. Argon, 1982; Cocks and Ashby, 1982; Riedel, 1987).

Creep crack growth experiments on test specimens show that a large variety of crack growth patterns can be observed, depending on the choice of material and crack tip geometry. Hayhurst, Dimmer and Morrison (1984) studied British Standard notched specimens, where crack growth was found to occur straight-ahead from the notch tip for aluminium and copper and under an angle of 40° for stainless steel. For sharp cracked specimens Hayhurst, Brown and Morrison (1984) found quite different behaviour: 55° inclined, isolated crack growth for

aluminium, diffuse damage in a wedge-shaped area for copper and meandering crack growth in the plane of the crack for stainless steel. More recently, Ozmat et al. (1991) focused on early stages of crack extension in stainless steel from both pre-fatigued cracks and blunt cracks with machined radii of curvature. They found an initially branched growth at 50° with the crack front for the sharp pre-fatigued cracks and straight-ahead growth for the blunt cracks. However, in later stages of growth for one pre-fatigued case the crack showed a tendency to become parallel to the initial crack front again. In contrast, the initial straight-ahead growth from the blunted cracks changed in a meandering mode of growth, associated with subsequent attempts of the crack to deviate from the roughly straight-ahead growth direction in the median plane. In a literature survey, Ozmat et al. (1991) found that similar transient stages of nonplanar crack growth were often observed, also for different materials. Such nonplanar propagation may retard crack growth and thus contribute substantially to the total lifetime.

The objective of the present study is to gain some understanding of the observed phenomena by actually simulating the intergranular, discrete nature of crack advance. To do so, we use a recently developed microstructural model for creep crack growth. The idea is to represent the near tip process zone by a collection of discrete grains. Grain boundary cavitation and sliding are allowed to occur along the grains and are accounted for by grain elements and grain boundary elements (Onck and Van der Giessen, 1997). To simulate creep crack growth a boundary layer approach is adopted, in which the discrete process zone is matched to a standard creeping, non-damaging continuum. Loading, specimen geometry and crack length are fully communicated through the boundary conditions, according to the C^* -controlled mode I HRR field. In a previous study (Onck and Van der Giessen, 1998a), it was demonstrated that this microstructural model is able to simulate macroscopic crack growth by the linking-up of microcracks, taking full account of the underlying microscopic mechanisms. Here, we investigate how the linking-up process, the crack growth rate and direction are affected by the initial crack tip radius. In addition, the influence of microstructural parameters like the diffusion parameter and grain boundary viscosity is studied, while also the effect of grain boundary shear stress on cavity growth and nucleation is incorporated.

2. Constitutive equations

The material model incorporates (i) elasticity and creep in the grains, and (ii) the nucleation, growth and coalescence of cavities on the grain boundaries, along with grain boundary sliding. The constitutive equations are similar to those used in a previous study (Onck and Van der Giessen, 1998a) and will therefore only be summarized here.

The material inside the grains is assumed to be homogeneous and isotropic, and is supposed to deform by elasticity and dislocation creep. The latter is described by the power law

$$\dot{\varepsilon}_e^C = B\sigma_e^n, \quad (1)$$

where B is the creep parameter, n is the creep exponent and σ_e is the effective Mises stress.

The cavitation process at the grain boundaries involves the nucleation, growth and coalescence of cavities (see e.g. Argon, 1982; Riedel, 1987). The cavities are characterized by their radius a , half-spacing b and spherical-caps shape determined by the cavity tip angle $\psi = 75^\circ$ (see Figure 1(a)). The average separation between two adjacent grains is $\delta_c = V/(\pi b^2)$ where V is the cavity volume $V = 4/3\pi a^3 h(\psi)$, with h the cavity shape parameter defined by $h(\psi) = [(1 + \cos \psi)^{-1} - \frac{1}{2} \cos \psi] / \sin \psi$. We adopt a smeared-out approach in which the

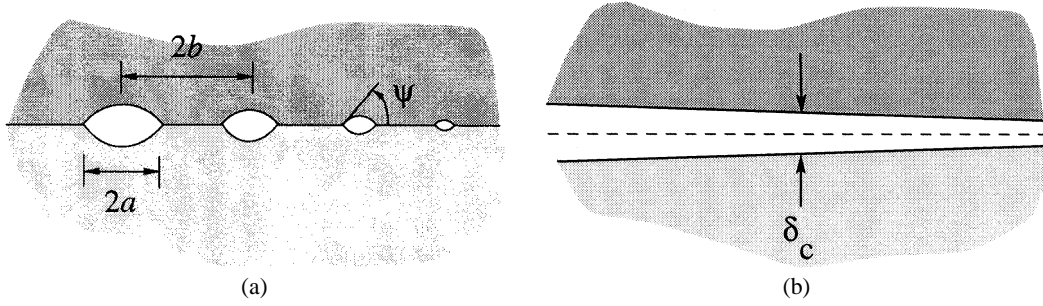


Figure 1. (a) Geometry of cavities in the spherical-caps shape; (b) 'Smeared-out' representation of grain boundary cavitation in terms of a continuous varying separation δ_c .

discrete distribution of cavities is replaced by a continuous distribution (see Figure 1(b)). The rate of separation between two adjacent grains,

$$\dot{\delta}_c = \frac{\dot{V}}{\pi b^2} - \frac{2V \dot{b}}{\pi b^2 b}, \quad (2)$$

is determined by the volumetric growth rate \dot{V} of the cavities and the rate of change of the cavity spacing \dot{b} .

The cavities grow by diffusion of atoms from their surface into the grain boundary layer and by creep deformation of the surrounding grain material. Needleman and Rice (1980) and Sham and Needleman (1983) investigated the combined influence of creep and diffusion on cavity growth by means of detailed finite element calculations. They summarized their numerical results into an expression for the volumetric cavity growth rate \dot{V} , which was later modified by Tvergaard (1984a) to become

$$\dot{V} = \dot{V}_{\text{diff}} + \dot{V}_{\text{creep}}, \quad (3)$$

where \dot{V}_{diff} is the contribution of diffusion

$$\dot{V}_{\text{diff}} = 4\pi \mathcal{D} \frac{\sigma_n}{\ln(1/f) - \frac{1}{2}(3-f)(1-f)}, \quad (4)$$

with

$$f = \max \left[\left(\frac{a}{b} \right)^2, \left(\frac{a}{a + 1.5L} \right)^2 \right], \quad (5)$$

and where the contribution of creep, \dot{V}_{creep} , is given by

$$\dot{V}_{\text{creep}} = \begin{cases} \pm 2\pi \dot{\epsilon}_e^c a^3 h(\psi) \left[\alpha_n \left| \frac{\sigma_m}{\sigma_e} \right| + \beta_n \right]^n, & \text{for } \pm \frac{\sigma_m}{\sigma_e} > 1; \\ 2\pi \dot{\epsilon}_e^c a^3 h(\psi) \left[\alpha_n + \beta_n \right]^n \frac{\sigma_m}{\sigma_e}, & \text{for } \left| \frac{\sigma_m}{\sigma_e} \right| \leq 1. \end{cases} \quad (6)$$

The coupling between diffusive and creep contributions to void growth enters in (5) through the stress and temperature dependent length scale

$$L = \left[\mathcal{D} \sigma_e / \dot{\varepsilon}_e^C \right]^{1/3}, \quad (7)$$

where \mathcal{D} is the grain boundary diffusion parameter. For small values of a/L (say, $a/L < 0.1$) cavity growth is dominated by diffusion, while for larger values of a/L , creep growth becomes more and more important. The range of validity of expression (3) was specified to be $a/L \leq 10$. The constants α_n and β_n in (6) are given by $\alpha_n = 3/(2n)$ and $\beta_n = (n-1)(n+0.4319)/n^2$. The effective stress σ_e , the mean stress σ_m and the normal stress σ_n in (4)–(7) are stresses remote from each cavity on the size scale of individual cavities, but are local quantities on the scale of grains.

The cavity spacing b changes in the course of the failure process due to the nucleation of new cavities and, to a lesser extent, due to finite strain effects associated with the in-plane deformations. In the deformed state, the cavity density is $1/\pi b^2$. Interpreting N as the density per unit undeformed grain boundary, it follows that the rate of change of b , to be substituted into (2), is determined by

$$\frac{\dot{b}}{b} = \frac{1}{2}(\dot{\varepsilon}_I + \dot{\varepsilon}_{II}) - \frac{1}{2} \frac{\dot{N}}{N}, \quad (8)$$

in terms of the in-plane principal logarithmic strain rates $\dot{\varepsilon}_I$ and $\dot{\varepsilon}_{II}$ at the grain boundary and the cavity nucleation rate \dot{N} .

The nucleation of cavities in high temperature applications occurs at very small length scales (see e.g. Raj and Ashby, 1975), which has hampered the understanding of the actual nucleation mechanism. Experimental observations during creep tests show that the density of cavities – above a certain size – increases in proportion to strain and that most cavities are observed on facets which are transverse to the tensile stress direction (see e.g. Dyson and McLean, 1977; Cocks and Ashby, 1982). Furthermore, it is often reported that the susceptibility to nucleation depends highly on the grain boundary microstructure, such as the distribution of second-phase particles, certain carbides and trace impurities (see Wu and Sandström, 1996, for an overview). Consensus has been reached in the literature on the fact that nucleation must be attributed to a stress-concentration mechanism that occurs throughout the creep life in proportion to strain. Mainly two sources for the stress concentrations have been identified: ledges or second phase particles at sliding grain boundaries (e.g. Argon et al., 1980) or the interaction of dislocations and glide planes with grain boundaries (e.g. Dyson, 1983; Lim, 1987). However, due to the complexity of the nucleation process and the lack of detailed experimental observations to back-up the models, a physically sound description of cavity nucleation is not yet available. Therefore, we adopt a phenomenological model that is consistent with experimental observations and motivated by Dyson's (1983) considerations.

We imagine that cavity nucleation is caused by the stress concentrations that result from the interaction of dislocations with the grain boundary. Following Dyson (1983), each increment of strain near the boundary is assumed to produce a number of decohesions (or nuclei), from which only those that have a radius above a certain critical value $r_{\text{crit}} = 2\gamma/\sigma_n$, determined by the surface free energy γ , become stable and do not sinter close. Thus, more nuclei become stable at facets which have a favourable tensile stress state. The resulting rate of cavity

nucleation is taken to be governed by the nucleation law, suggested by Van der Giessen and Tvergaard (1990)

$$\dot{N} = F_n \left(\frac{\sigma_n}{\Sigma_0} \right)^2 \dot{\varepsilon}_e^C, \quad \text{for } \sigma_n > 0, \quad (9)$$

where Σ_0 is a normalization factor and F_n a material parameter that incorporates the microstructural features that influence the rate of nucleation at a grain boundary. For instance, grain boundary particles and trace impurities tend to decrease the surface free energy γ and thus the critical radius r_{crit} . This is incorporated through an enhanced nucleation activity F_n , so that per increment of strain more cavities are nucleated (see e.g. Needham and Gladham, 1986).

The grain boundary nucleation law (9) implies that cavity nucleation at any facet (independent of the nucleation activity F_n) occurs right from the first stages of plastic deformation. This is not in accordance with nucleation experiments which often show that the number of cavitating facets increases with strain (see e.g. Chen and Argon, 1981), meaning that nucleation on some facets occurs only late in creep life, if it occurs at all. To incorporate this, we postulate that a certain threshold value must be overcome before grain boundary nucleation can effectively take place. Since the nucleation rate in (9) depends on strain rate as well as stress, we define a combined stress/accumulated strain quantity, $S = (\sigma_n/\Sigma_0)^2 \dot{\varepsilon}_e^C$, which must have reached a threshold value, S_{thr} , before cavity nucleation is triggered. Rather than treating S_{thr} as a separate parameter, we assume that it is related to F_n through

$$S_{\text{thr}} = N_I / F_n. \quad (10)$$

Thus, when the nucleation activity is high (F_n is large), the threshold value is low and vice versa. The parameter N_I in (10) is the nonzero cavity density on a facet at the moment that nucleation is triggered, i.e. once the nuclei have attained a super-critical size. For a homogeneous material under constant stress (i.e. $\dot{S} = (\sigma_n/\Sigma_0)^2 \dot{\varepsilon}_e^C$), this choice ensures that (9) is consistent with the observation that the cavity density is proportional to creep strain. Finally, since experiments show that the cavity density tends to saturate at large creep strains, we assume that the nucleation of new cavities stops as soon as N reaches a value N_{max} (see e.g. Dyson and McLean, 1977).

An appropriate way to quantify the damage state at a facet is the parameter a/b . From the definition of the cavity volume V it follows that the cavity growth rate is given by $\dot{a} = \dot{V}/(4\pi a^2 h(\psi))$ and together with (8) this describes the damage evolution. When the ratio a/b approaches unity, coalescence of cavities occurs. However, experimental observations suggest that coalescence may occur earlier by ductile tearing or by cleavage of the ligament between the cavities (e.g. Cocks and Ashby, 1982). Like Van der Giessen and Tvergaard (1994), we assume coalescence to take place at $a/b = 0.7$.

Another important mechanism at high temperatures is grain boundary sliding. Due to the disordered structure of grain boundaries, the shear resistance can be low compared to the resistance of the grain material, which causes the grain boundary shear stresses to relax. Ashby (1972) suggested to model the grain boundaries as thin layers that slide in a Newtonian viscous manner, governed by

$$\dot{u}_s = w \frac{\tau}{\eta_B}, \quad (11)$$

where \dot{u}_s is the relative sliding velocity of adjacent grains due to a shear stress τ and w is the thickness of the boundary. The grain boundary viscosity η_B can be related to the grain boundary diffusivity, while irregularities in the grain boundary, such as ledges or second-phase particles, can increase the boundary viscosity. However, in this paper, η_B/w is regarded as a separate material parameter, which can be expressed in terms of the strain-rate parameter (Ghahremani, 1980)

$$\dot{\epsilon}_B = \left(\frac{w B^{-1/n}}{d \eta_B} \right)^{n/(n-1)}, \quad (12)$$

with d a length parameter, that will be related to the grain size later on. The relative importance of the grain boundary sliding as a deformation mechanism is governed by the ratio $\dot{\epsilon}_e^C/\dot{\epsilon}_B$. Free sliding ($\eta_B = 0$) corresponds to $\dot{\epsilon}_e^C/\dot{\epsilon}_B = 0$, while no sliding ($\eta_B \rightarrow \infty$) is equivalent to $\dot{\epsilon}_e^C/\dot{\epsilon}_B \rightarrow \infty$.

3. Small-scale damage model

The numerical model used in this paper is similar to that proposed by the authors in (Onck and Van der Giessen, 1998a) and the reader is referred to this paper and the references therein for details.

We consider a mode I crack in an extensively creeping material. For a power law creeping material as described by (1) the asymptotic stress field is the HRR-field given by

$$\sigma^{ij} = \left[\frac{C^*}{BI_n r} \right]^{1/(n+1)} \tilde{\sigma}^{ij}(\theta, n). \quad (13)$$

Here, r and θ are polar coordinates centered at the initial crack tip, C^* the time-dependent version of the J -integral and I_n an n -dependent dimensionless constant. The dimensionless functions $\tilde{\sigma}^{ij}(\theta, n)$ and constant I_n have been tabulated by Shih (1983).

To simulate creep crack growth, a boundary layer approach is adopted, assuming that damage remains located to the crack tip and that the specimen geometry, crack length and remote loads are fully communicated through the amplitude C^* of the near-tip singular field. Figure 2(a) shows the circular domain of the boundary value problem under consideration (symmetry conditions along the crack plane are assumed). This ‘far-field’ region is discretized using standard continuum elements accounting for elasticity and creep. Near the crack tip a process window is identified (Figure 2(b)), in which the material is built up as an aggregate of discrete hexagonal grains, with an initial facet width of $2R_f$. Each grain is represented by a special-purpose, six-noded element – that we termed grain element – which accounts for elasticity and creep. The grain elements are connected by grain boundary elements that account for the nucleation, growth and coalescence of grain boundary cavities, while also grain boundary sliding is incorporated. Details about this grain element method can be found in (Onck and Van der Giessen, 1997). It suffices here to note that in this type of modelling all quantities related to grain boundary damage on a grain boundary facet are uniform over that facet.

The small-scale damage assumption is satisfied by taking the dimensions of the process window (A_0, B_0) small compared to the radius r_0 of the circular domain: $A_0 = r_0/100$. Most

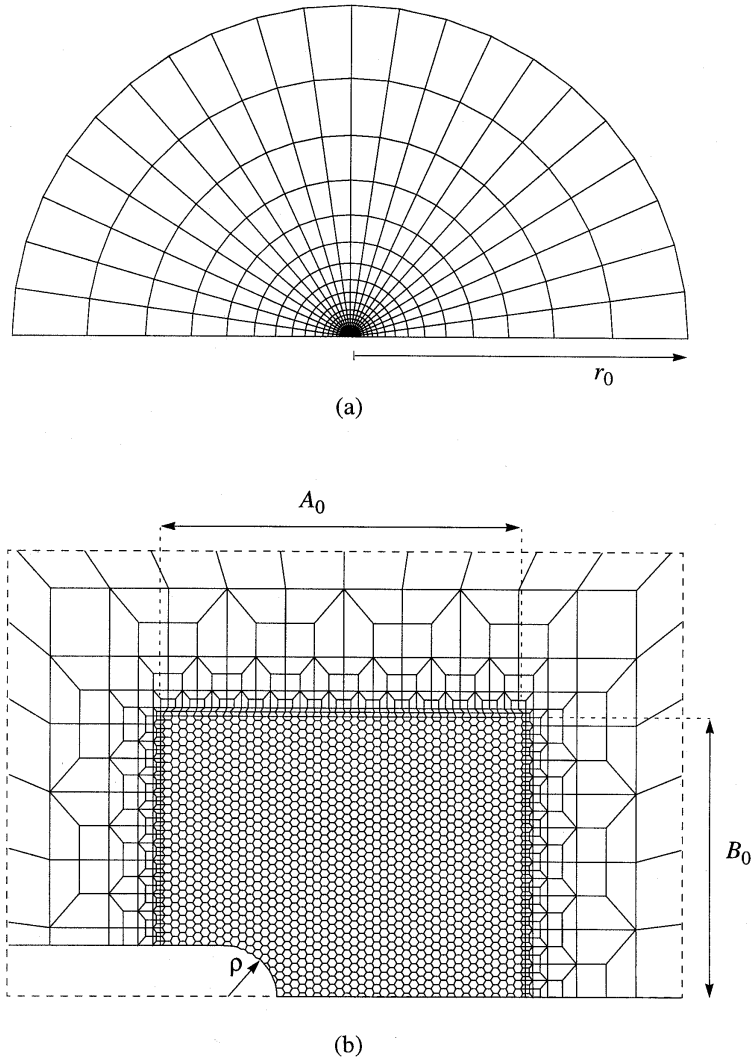


Figure 2. Finite element mesh used for small-scale damage analysis. (a) Circular domain with radius r_0 . (b) Blunted crack tip region, showing the process window with dimensions A_0 , B_0 , consisting of grain elements and grain boundary elements. Cavitation damage is allowed to occur along all grain boundaries in the process window, containing 48×33 grains.

results to be presented are for an initially blunt crack tip with a radius of $\rho = 12\sqrt{3}R_I$ (see Figure 2(b)), but also a sharp crack $\rho \rightarrow 0$ is considered as a limiting case.

We assume that all initial elastic transients have relaxed before damage at the crack tip develops. Therefore, the HRR-field is not only prescribed as a remote boundary condition, but also as an initial condition. Clearly, since the HRR-field is only valid for a sharp crack, some time is needed for the blunted crack case before the stress field around the notch has converged to a steady-state solution. In the numerical analysis, grain boundary cavitation starts once convergence to this field has been achieved.

4. Recapitulation of sharp crack results

Before analyzing a blunted crack tip, we summarize some essential features from a previous study (Onck and Van der Giessen, 1998a) on the damage evolution from a sharp crack, which will serve as a reference point for the blunted crack analysis.

The process of creep crack growth as prescribed in the previous sections can be expressed in terms of the following set of non-dimensional parameters (subscript R indicates reference values, I indicates initial values)

$$\left\{ n, \frac{\Sigma}{E}, \frac{\dot{E}_e^C}{\dot{\epsilon}_B}, \frac{N_I}{N_R}, \frac{a_I}{R_I}, \frac{L_R}{R_I}, \frac{F_n}{N_R} \right\}, \quad (14)$$

with $N_R = 1/(\pi R_I^2)$. The reference stress Σ is taken to be the amplitude of the HRR-field at a distance R_I from the tip: $\Sigma = [C^*/BI_n R_I]^{1/(n+1)}$. The creep reference time $t_R = 1/\dot{E}_e^C$, with $\dot{E}_e^C = B\Sigma^n$, is used to normalize time. The competition between creep and diffusion is monitored by the length scale parameter $L_R = (\mathcal{D}\Sigma/\dot{E}_e^C)^{1/3}$, defined in terms of the reference stress Σ , in accordance with (7). We use $n = 5$ and assume that the load level C^* is such that the elastic strains remain small: $\Sigma/E = 0.9 \times 10^{-3}$. Furthermore, we specify $a_I/R_I = 0.67 \times 10^{-3}$, $N_I/N_R = 40$, $N_{\max}/N_R = 100$, while for the length parameter d in (12) we take the diameter of a circle whose area is the same as a grain, i.e. $d = 3.64R_I$. An intermediate value for the grain boundary viscosity η_B/w is chosen such that $\dot{E}_e^C/\dot{\epsilon}_B = 10$. As in (Onck and Van der Giessen, 1998a) the resulting strain rate enhancement due to the viscous grain boundary sliding (see e.g. Crossman and Ashby, 1975) is incorporated through an enhanced value for the creep parameter B .

The relative contributions of diffusion, creep and nucleation to the cavitation damage process determine the characteristic features of crack growth. Assuming that cavity growth is mainly driven by diffusion, the relative rates of diffusion and creep expressed through L_R determine whether cavitation is constrained by creep or not (Dyson, 1976). For any given value of Σ (and, hence, \dot{E}_e^C), a large value of L_R corresponds to relatively rapid diffusion; creep is too slow to readily accommodate the damage accumulation, thus leading to creep constrained cavitation growth and relatively brittle fracture. Smaller values of L_R tend to lead to more ductile behaviour with the creep strains and the crack opening being more significant. Since variations in the diffusion parameter \mathcal{D} scale as L_R^3 , the range of values of L_R that lead to realistic failure strains is quite narrow. The previous study (Onck and Van der Giessen, 1998a) has employed two values that lead to either rather brittle failure, $L_R/R_I = 0.1$, or rather ductile failure, $L_R/R_I = 0.032$. To maintain the connection with this study, we will consider the same values here and, for conveniency, identify them as values for the brittle or ductile cases. The parameter L_R relates diffusion to creep, while the parameter F_n couples the creep rate to the nucleation rate (see (9)). Treating these two parameters as independent ones may eventually lead to unrealistically small cavity densities at the moment of coalescence. To resolve this, we assume that the nucleation activity F_n is related to the diffusion parameter \mathcal{D} , leading to $F_n/N_R = 5.3 \times 10^4$ and $F_n/N_R = 2.4 \times 10^3$ for the brittle ($L_R/R_I = 0.1$) and ductile case ($L_R/R_I = 0.032$), respectively. Unless stated otherwise, all grain boundary facets in the process zone are assigned the same value of F_n .

Before looking at the damage evolution, we consider the initial HRR-stress distribution near the sharp crack tip. Observation of the constitutive equations in Section 2 yields that the principal driving forces for grain boundary cavitation are the normal facet stresses and

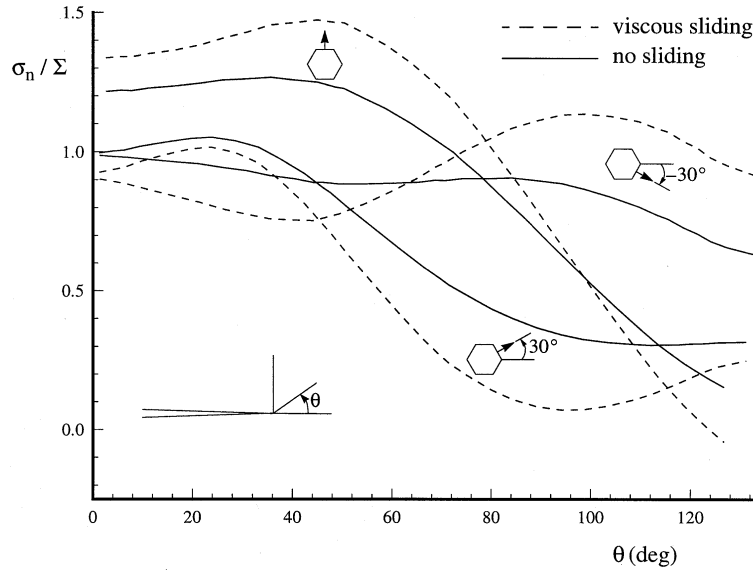


Figure 3. Angular distribution of the normal facet stresses at the three grain boundary facet orientations at $r = 10d$ from a sharp crack tip.

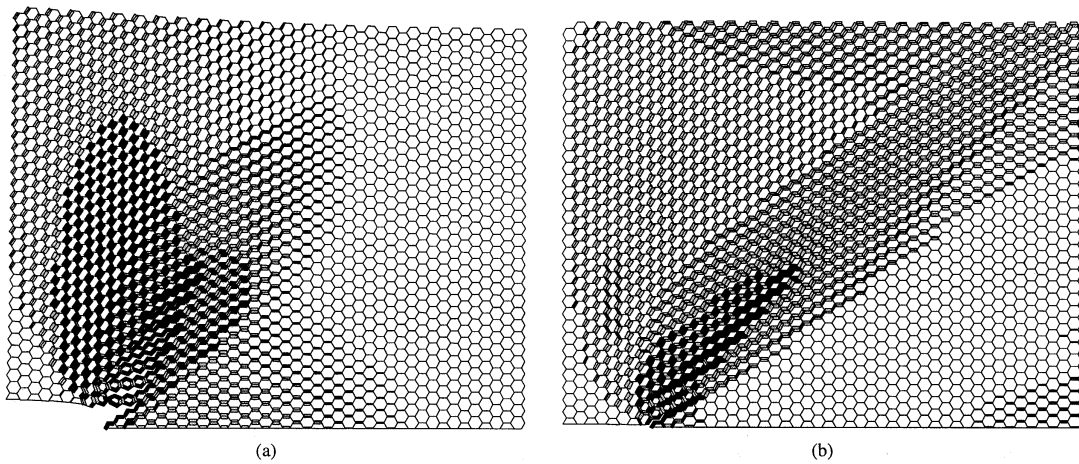


Figure 4. Grain boundary cavitation state in the process window for the sharp crack analysis. Values of a/b are plotted along and on either side of the facets. Microcracked facets, where $a/b = 0.7$, are highlighted in black. (a) $L_R/R_I = 0.032$, $t/t_R = 1.86$ (b) $L_R/R_I = 0.1$, $t/t_R = 0.14$ [From Onck and Van der Giessen, 1998a].

creep deformation. Figure 3 shows the angular distribution of the normal stress σ_n at 10 grain distances d from the crack tip for no-sliding ($\dot{E}_e^C/\dot{\epsilon}_B \rightarrow \infty$) as well as for viscous-sliding ($\dot{E}_e^C/\dot{\epsilon}_B = 10$) conditions. From the no-sliding field, which is similar to the standard HRR-field, we see that the stresses are highest at horizontal facets for small values of θ , while for larger θ -values the facets at -30° with the crack front are subject to the highest stresses. The effect of a lower grain boundary viscosity is that the shear stresses at the grain boundaries relax, resulting in a stress redistribution that appears to leave the angular distribution unaffected, but sheds even more load on horizontal and -30° facets. For the HRR-field, the effective stress and the creep rate concentrate above the crack tip, reaching its maximum at $\theta = 96^\circ$.

Figures 4(a, b) show snapshots of the damage state in the process window for the sharp crack for the ductile ($L_R/R_I = 0.032$) and brittle ($L_R/R_I = 0.1$) case, respectively. The cavitation state is shown by plotting the value of a/b perpendicular to each facet and with the ordinate along the facet. Figure 4(a) shows that the crack propagates along a $\sim 60^\circ$ direction with the crack plane by the linking-up of facet-sized microcracks. Two families of microcracks can be observed: horizontal microcracks are located predominantly in front of the initial crack tip position, while inclined cracks (oriented at -30° with the crack front) are formed more above the crack tip where the creep rate and the nucleation rate are highest. The actual crack growth occurs in a region where these two families meet. These observations can be traced back quite well to the initial distribution of creep rate and normal facets stresses as depicted in Figure 3. This is a direct consequence of the fact that cavitation development for the ductile case is not constrained by creep deformation, leaving the HRR-stress distribution rather undisturbed during the initial stages of cavitation development, until the moment of cavity coalescence and microcracking. Figure 4(b) corresponds to $L_R/R_I = 0.1$, indeed showing that the crack growth process is more brittle than in Figure 4(a). The crack grows at approximately 50° along a rather narrow band of extensive damage, which is a result of stress redistributions away from the initial crack tip as grain boundary cavitation develops. The stress redistributions are due to the active creep constraint on cavitation (Dyson, 1976).

5. Results

5.1. CONSTRAINED VS. UNCONSTRAINED CAVITATION

In this section we analyze creep crack growth from a blunted crack tip, using the mesh of Figure 2(b) with a crack tip radius $\rho = 12\sqrt{3}R_I$. To compare the results with the sharp crack case, discussed in the previous section, we use the same set of dimensionless parameters, similarly making a distinction between ductile ($L_R/R_I = 0.032$) and brittle ($L_R/R_I = 0.1$) crack growth. Of course, for a blunted crack the results are also dependent on the size of the crack tip radius, so that ρ/R_I comes in as an additional parameter in the dimensionless set (14).

Before looking at damage development, we first analyze how the blunting affects the initial stress distribution around the crack tip as compared with the HRR-field of the sharp crack. Figure 5 shows the effective stress at $r/\rho = 1.2, 1.8, 4.4$ and 87.5 . Close to the crack tip, the effective stress reaches a maximum at $\theta = 0$, and converges to the HRR-distribution (maximum at $\theta = 96^\circ$) further away from the tip. The convergence to the HRR-field remote from the blunt crack tip is illustrated in Figure 5 by including the HRR dimensionless effective stress field $\tilde{\sigma}_e$, corresponding to (13). Clearly, the HRR-singularity (13) is not valid in a region within a number of notch root diameters from the tip. Figure 6 shows the normal facet stresses at $r = 10d = 1.8\rho$, similar to Figure 3 for the sharp crack. Stresses are highest on horizontal facets in front of the crack (small θ) and at -30° facets for larger θ values. When grain boundary sliding is active, load is redistributed from the 30° facets to the horizontal facets for small θ , and from horizontal facets to -30° facets for higher values of θ . Compared to the sharp crack stress field of Figure 3 two observations can be made: (i) the stresses on 30° facets drop considerably in the median plane of the crack, which is a direct result of the lower hydrostatic stress state in front of blunt notches; (ii) the peak stresses on the horizontal and the -30° facets shift towards smaller values of θ , with the intersection moving from $\theta \approx 80^\circ$ for the sharp crack (cf. Figure 3) to $\theta \approx 30^\circ$ for the blunted crack.

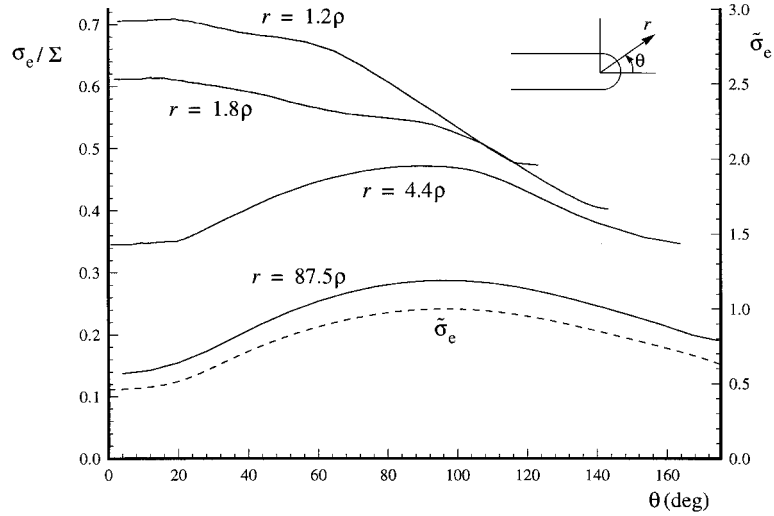


Figure 5. Angular distribution of the effective stress at four distances from the center of the circular region of the blunted crack tip. Also the dimensionless effective stress $\tilde{\sigma}_e$ is plotted, which corresponds to the HRR-field in (13).

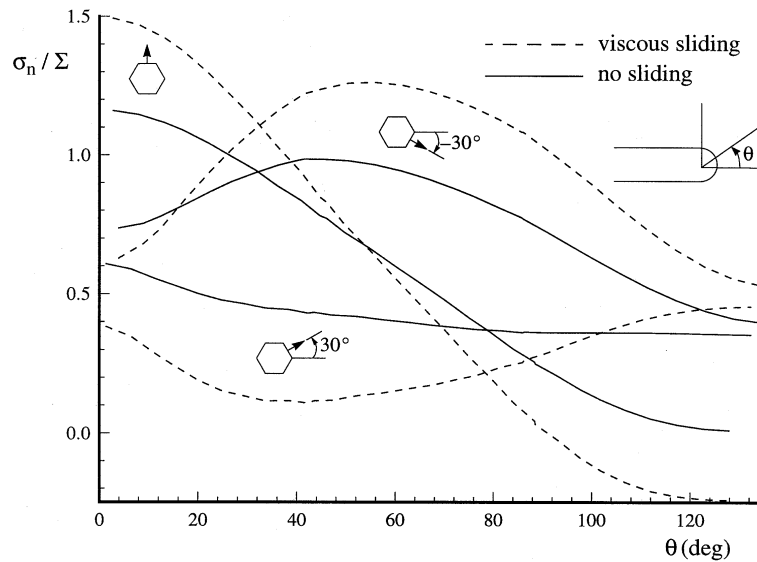


Figure 6. Angular distribution of the normal facet stresses at the three grain boundary facet orientations in a hexagonal microstructure at $r = 10d = 1.8\rho$ for the blunted crack tip.

Figure 7 shows the grain boundary cavitation state along with the effective stress distribution for the ductile case ($L_R/R_I = 0.032$) at two instances during crack extension. In Figure 7(a), cavity nucleation and subsequent cavity growth has occurred on -30° facets above the notch and on horizontal facets in the median plane in front of the crack tip. Microcracks have formed in two separate regions, where facet normal stresses are highest (cf. Figure 6). The actual crack extension (see Figure 7(b)), however, takes place along a 30° direction in an area in between these regions, where conditions are favourable for linking-

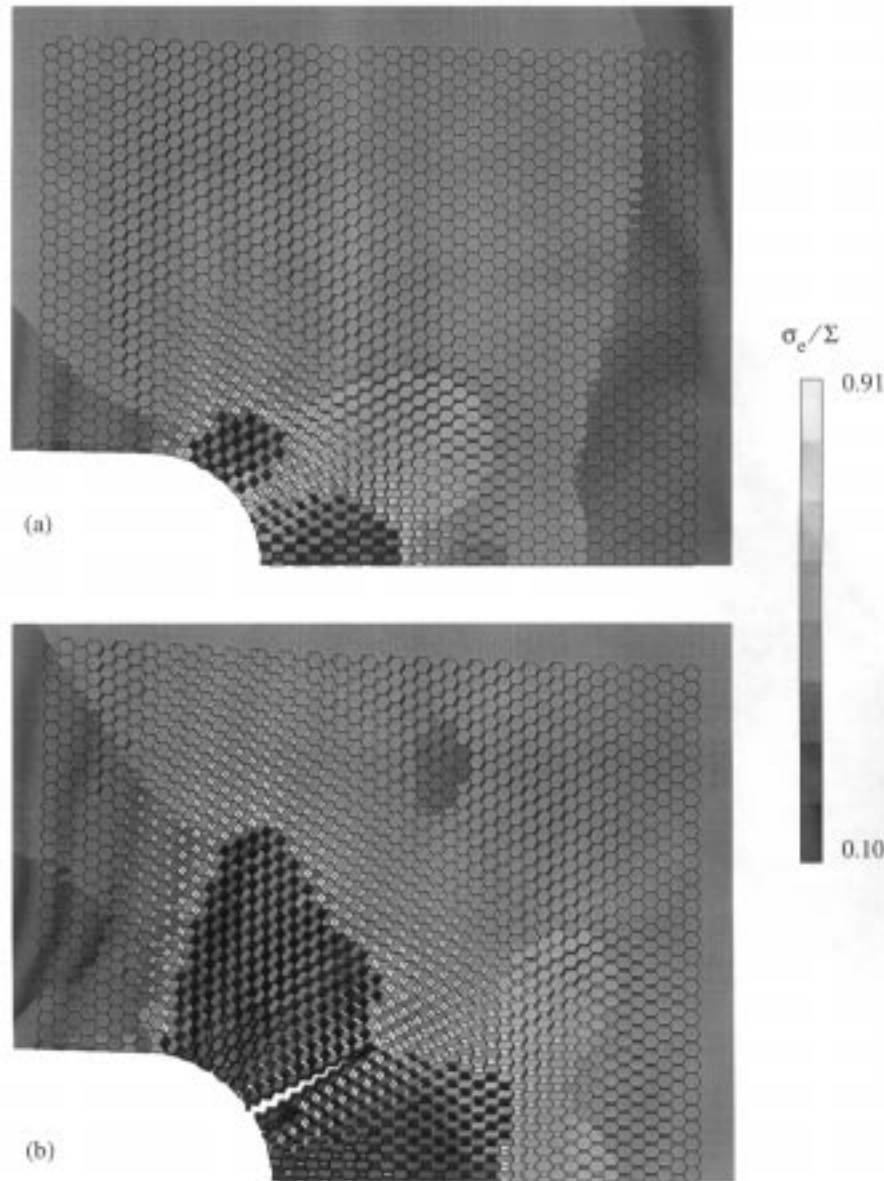


Figure 7. Grain boundary cavitation state and effective stress distribution in the process window (see Figure 2(b)) for $L_R/R_I = 0.032$ at two instances during early crack extension. (a) $t/t_R = 1.12$; (b) $t/t_R = 1.92$.

up of microcracks. This $\sim 30^\circ$ direction coincides with the direction where the facet normal stresses on horizontal and -30° facets are equal (cf. Figure 6).

The next case analyzed corresponds to a larger value of the diffusion parameter \mathcal{D} , leading to $L_R/R_I = 0.1$. Figure 8 shows two snapshots of the damage development and stress state, similar to Figure 7. The same two families of cavitating facets can be distinguished as in the previous case, but damage and effective stress tend to concentrate in a rather narrow band along the 30° direction. Subsequent microcracking indeed occurs in this band, as shown in Figure 8(b). Clearly, for this brittle case, cavitation is constrained by creep of the surrounding

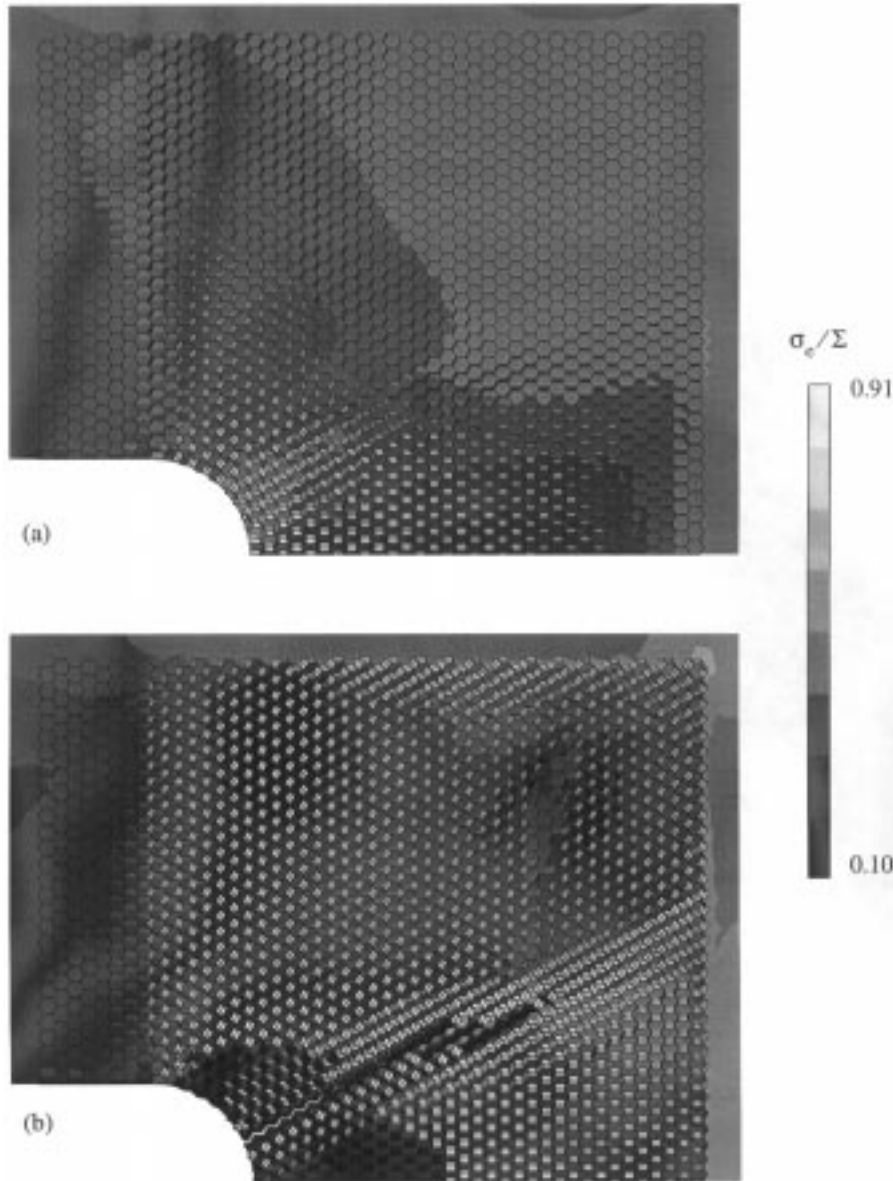


Figure 8. Grain boundary cavitation state and effective stress distribution in the process window for $L_R/R_I = 0.1$ at two instances during early crack extension. (a) $t/t_R = 0.06$; (b) $t/t_R = 0.18$.

grain material (Dyson, 1976). As a result, stresses redistribute to undamaged material as soon as cavities nucleate and start to grow. This can be clearly seen in Figure 8(a) where the stresses have relaxed in zones where cavitation has formed, even before microcracking has taken place. In contrast, in the more ductile, unconstrained case shown in Figure 7, stress relaxation only occurs in microcracked regions. In cases like in Figure 8, one should expect that the finite size of the process window will affect the crack growth characteristics due to the continuous stress re-distributions away from the damage zone. In a previous study, however, this effect has been investigated by taking different sizes for the process window and the effect was found to be very small (Onck and Van der Giessen, 1998a).

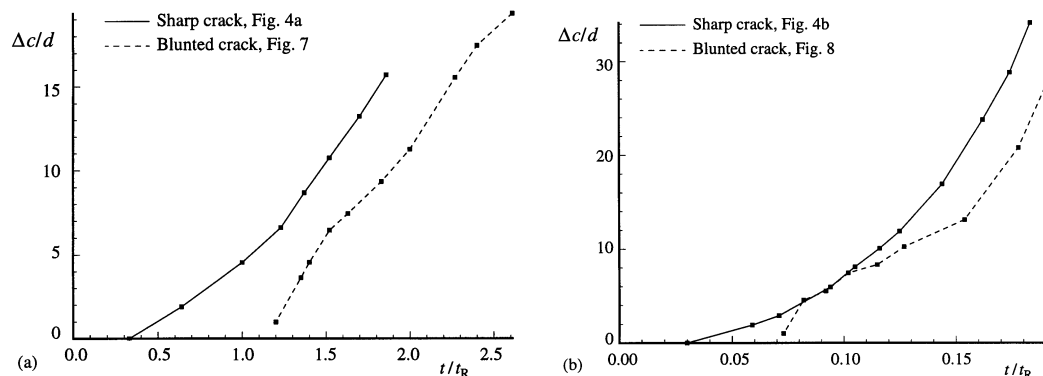


Figure 9. Crack extension $\Delta c/d$ vs. time t/t_R for a sharp and blunt crack tip. (a) Ductile case, $L_R/R_I = 0.032$; (b) Brittle case, $L_R/R_I = 0.1$.

Next, we investigate how crack tip blunting influences the initial crack growth rate by monitoring the crack extension $\Delta c/d$ as a function of time t/t_R . Figure 9(a) corresponds to the ductile case, including results of the sharp crack (see Figure 4(a)) with the blunt crack (see Figure 7). In comparing the results, it should be noted that Δc is measured along the direction of crack growth, which is $\sim 60^\circ$ for the sharp case and $\sim 30^\circ$ for the blunted case. It is seen that the incubation time for the blunted crack is roughly three times larger than for the sharp crack. This incubation time for the blunt crack consists of a period in which there are no microcracks (until $t/t_R = 0.79$) plus a period in which microcracking occurs only above and below the 30° direction of crack propagation (until $t/t_R \approx 1.12$, see Figure 7(a)). In contrast, for the sharp crack case, first microcracking occurs simultaneous with initial crack extension. The sharp crack extension goes through a period of accelerated growth after which the growth rate reaches a constant value, which is comparable to the growth rate of the blunted crack. Similar observations hold for the brittle case in Figure 9(b), although crack growth for the blunt crack shows an initial acceleration after which it decreases and increases again until it is approximately similar to the sharp crack growth rate. A satisfactory explanation of this behaviour has not yet been found.

5.2. FREE GRAIN BOUNDARY SLIDING

In order to briefly investigate the influence of the grain boundary viscosity, we adopt the set of material parameters for the ductile case ($L_R/R_I = 0.032$), but assume the grain boundary viscosity to be negligible, corresponding to $\dot{E}_e^C/\dot{\epsilon}_B = 0$. The initial stages of damage development are comparable to the case with $\dot{E}_e^C/\dot{\epsilon}_B = 10$, approximately until the moment associated with Figure 7(a). Then, however, damage starts to localize simultaneously in three directions as shown in Figure 10. The ‘localization band’ perpendicular to the crack plane also developed in the sharp crack case (Onck and Van der Giessen, 1998a), but here two additional bands form along 30° directions: one starting at the top of the notch and the other from the intersection of notch and midplane. This behaviour is a consequence of the regular 2-D microstructure in combination with free grain boundary sliding. The hexagonal grain aggregate naturally exhibits three ‘weak’ directions: $\theta = 30^\circ$, 90° and 150° . After some initial microcracking, which acts as a perturbation of the initial stable state, localization in the $\theta = 30^\circ$ and 90° directions becomes dominant. We have repeated the calculation with

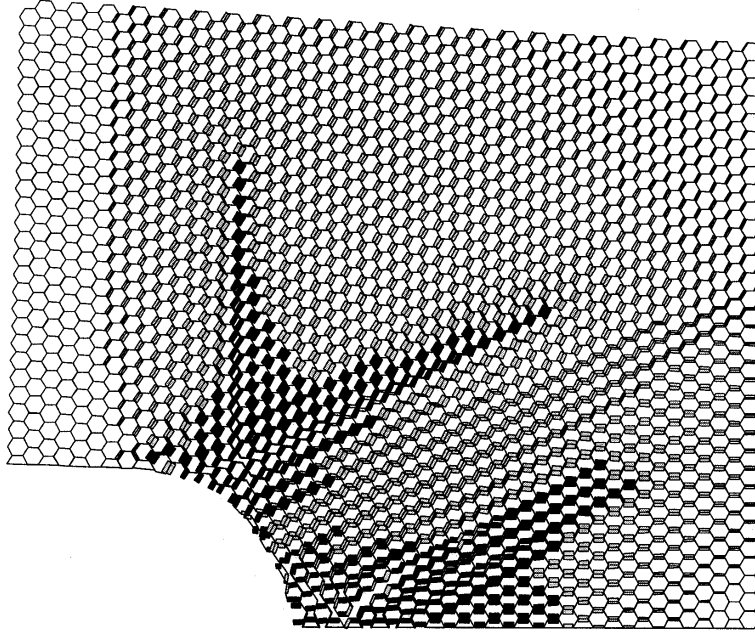


Figure 10. Damage state at $t/t_R = 2.25$ for $L_R/R_I = 0.032$ and free grain boundary sliding, $\dot{E}_c/\dot{\epsilon}_B = 0$.

the microstructure rotated over 90° , thus rendering the $\theta = 0^\circ$, 60° and 120° directions to be weak. Then, localization of damage was found to develop in the $\theta = 0^\circ$ and $\theta = 60^\circ$ directions.

5.3. RANDOM NUCLEATION

Experimental observations often show that nucleation on some facets occurs earlier and faster than on other, equally-oriented facets (e.g. Don and Majumdar, 1986; Wu and Sandström, 1996). This is incorporated here by randomly assigning the nucleation activity F_n to the various facets according to a Gaussian distribution. Then, through (10), also the threshold value S_{thr} for nucleation is randomly distributed, so that facets that nucleate fast also nucleate early. We focus again on the ductile ($L_R/R_I = 0.032$) and brittle ($L_R/R_I = 0.1$) case, where the mean values of the normal distribution for F_n are taken to be equal to the uniform values ($F_n/N_R = 2.4 \times 10^3$ and $F_n/N_R = 5.3 \times 10^4$, respectively) and where the standard deviations are taken equal to the respective mean values.

Figure 11(a) shows the stress and damage state for the ductile case at $t/t_R = 1.10$. Comparison with Figure 7(a) shows that damage development is much more diffuse, but that microcracking occurs first in the same areas. In Figure 11(b) it can be seen that, similar to Figure 7(b), the linking-up of microcracks proceeds most readily in an area in between the zones of first microcracking. Isolated regions of linked microcracks develop in the 30° direction, which subsequently link-up to form the actual ‘macroscopic’ crack, oriented at approximately 30° with the initial crack plane. Figure 12, for the brittle case, corresponds to Figure 8, but with the nucleation parameter F_n distributed randomly, using the same random realization as in Figure 11. Figure 12(a) depicts the early damage and stress state, showing that isolated facets have started to cavitate, resulting in a rather non-uniform stress distribution. This is due to the active creep constraint on cavitation, causing the normal stresses at cavitating

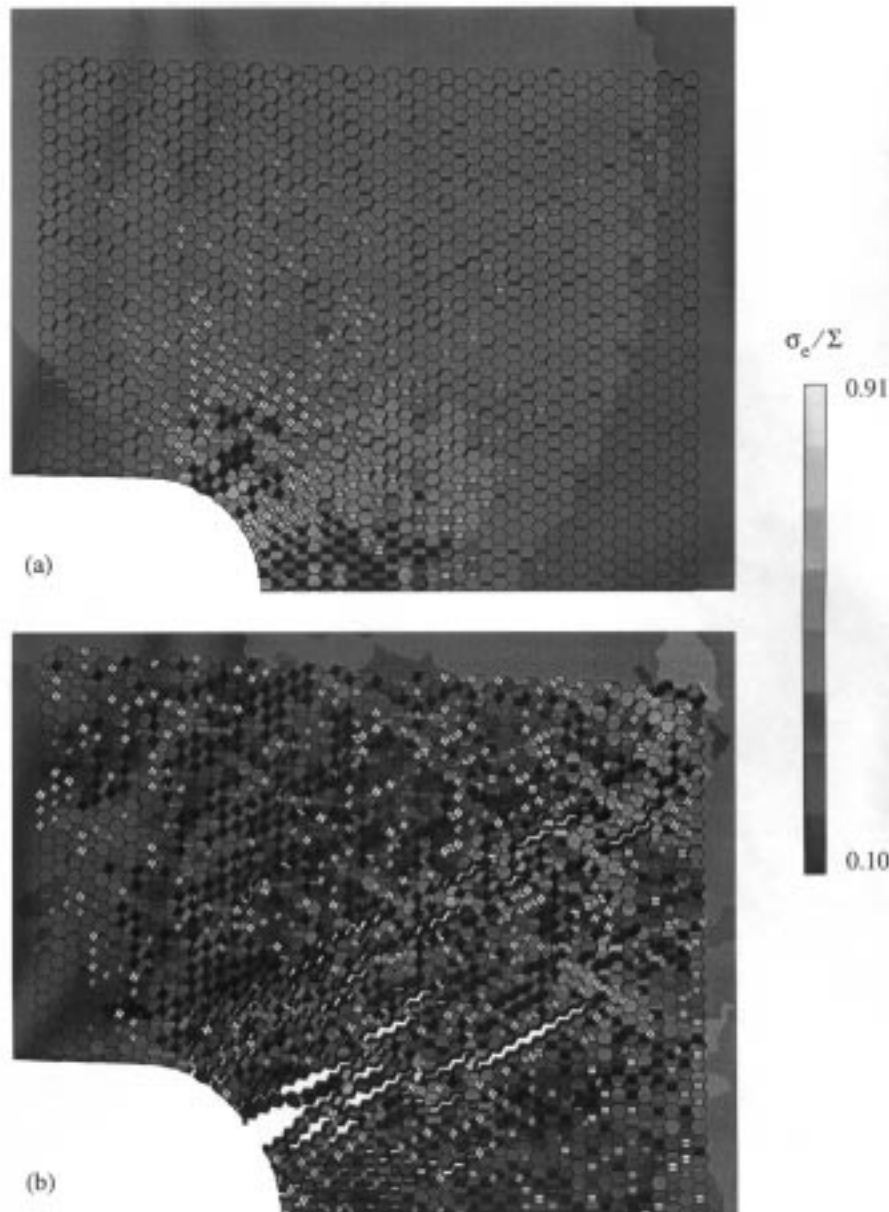


Figure 11. Grain boundary cavitation state and effective stress distribution at two instances during crack extension for $L_R/R_I = 0.032$ with a random distribution of F_n . (a) $t/t_R = 1.10$; (b) $t/t_R = 2.77$.

facets to relax, and shedding load to neighbouring, uncavitated regions. As a result, also these uncavitated regions start to cavitate, yielding a rather uniformly damaged region near the crack tip. Subsequent crack growth occurs by the joining of $\sim 30^\circ$ regions of linked microcracks, following a similar path as in Figure 11.

We have repeated the above two calculations for a different random realization, but with all other parameters unchanged (including the mean and standard deviation). Figures 13 and 14 correspond to Figures 11 and 12, respectively, and show that similar trends can be observed although the actual damage distributions are different.

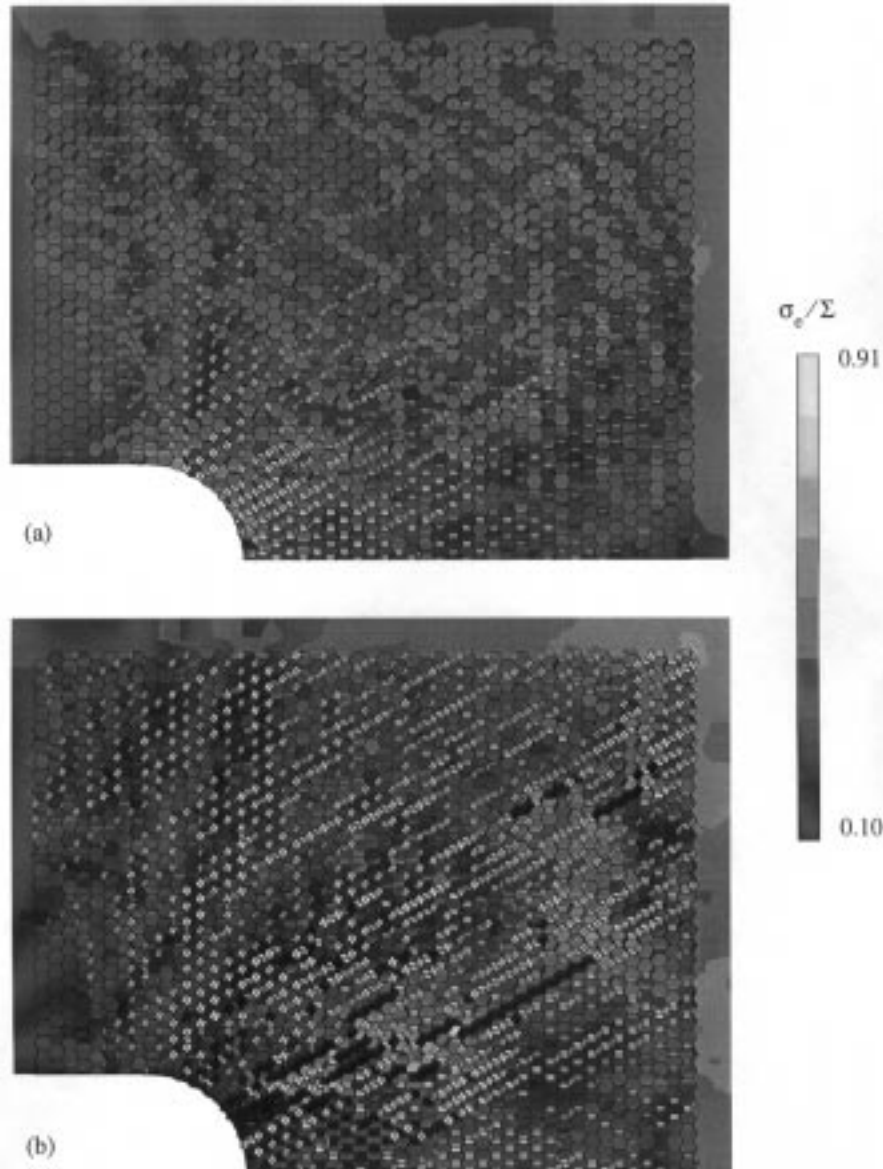


Figure 12. Grain boundary cavitation state and effective stress distribution at two instances during crack extension for $L_R/R_I = 0.1$ with a random distribution of F_n . (a) $t/t_R = 0.06$; (b) $t/t_R = 0.15$.

In experimental studies, polished sections are often investigated to analyze the damage state (e.g. Ozmat et al., 1991). The damage zone is then usually associated with more or less opened-up microcracks. To make a connection with such micrographs, we have plotted only the deformed geometry with the crack opening and microcracked regions painted black. Figure 15(a) shows such a micrograph, corresponding to Figure 11(b). Clearly, the two families of horizontal and inclined microcracks can be identified as well as the isolated 30° regions of linked microcracks. For comparison, Figure 15(b) shows a similar representation for a sharp crack at the same instant ($t/t_R = 2.73$), obtained for exactly the same parameters (Onck and Van der Giessen, 1998a). For a fair comparison, even the same random distributions of

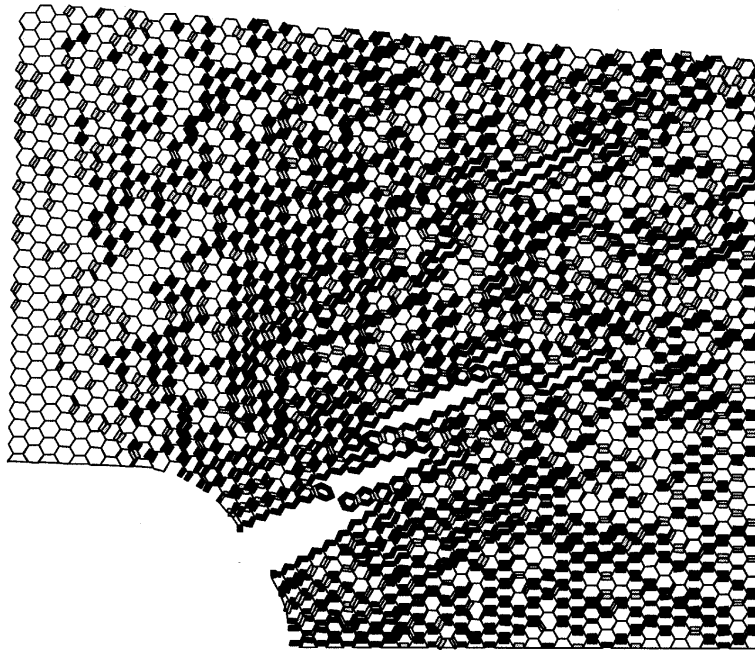


Figure 13. Grain boundary cavitation state at $t/t_R = 3.27$ similar to Figure 11, but with a different distribution of F_n .

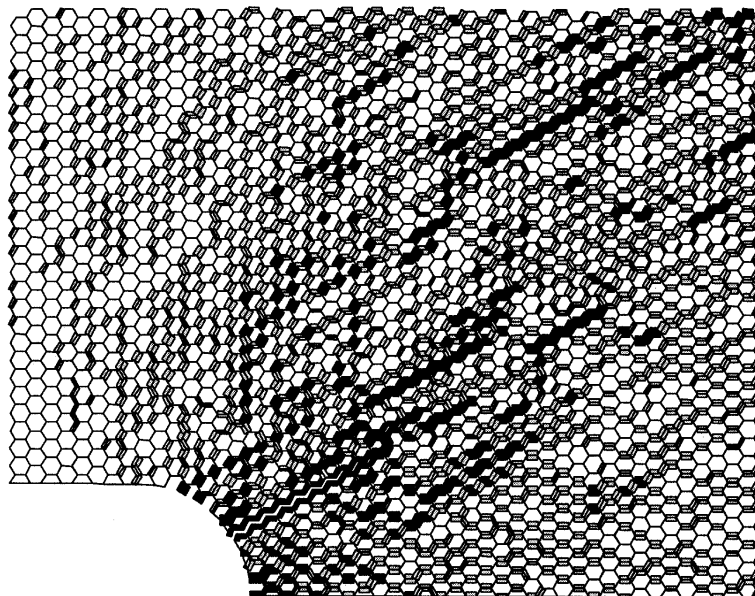
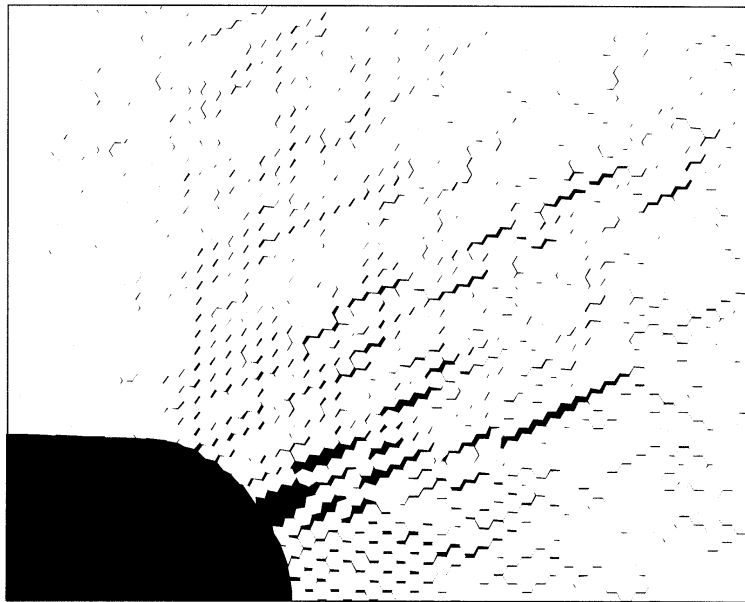
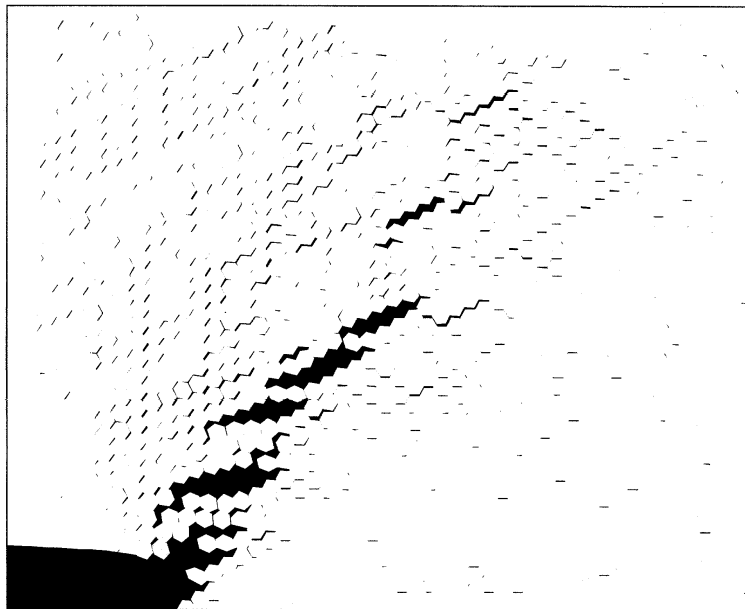


Figure 14. Grain boundary cavitation state at $t/t_R = 0.21$ similar to Figure 12, but with a different distribution of F_n (but similar to Figure 13).



(a)



(b)

Figure 15. 'Micrographs', where the crack opening and microcracked regions are painted black. (a) Blunted crack tip, corresponding to Figure 11(b); (b) Sharp crack tip at $t/t_R = 2.73$ [From (Onck and Van der Giessen, 1998a)].

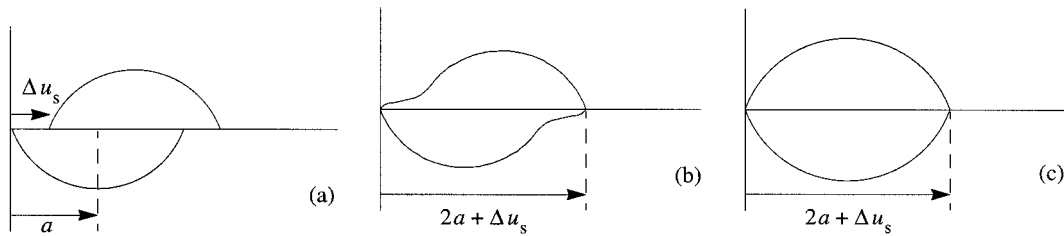


Figure 16. (a) Disturbance of the initial quasi-equilibrium void shape with radius a due to a sliding displacement Δu_s ; (b) Non-equilibrium void shape; (c) Restored quasi-equilibrium void shape with increased volume.

F_n were used; that is, the value of F_n at any grain facet in the microstructure with the blunt crack is the same as that at the corresponding facet in the material with the sharp crack. Two characteristic differences between the sharp and blunted crack case can be observed. Firstly, the crack growth direction has shifted from approximately 55° to 30° for the sharp and blunt crack, respectively. Secondly, for the sharp crack, crack growth has occurred along a rather narrow band of intense damage, while for the blunted crack, damage development and subsequent crack growth takes place in a more diffuse region. This is a result of the higher stress singularity at the sharp crack, concentrating creep strain and nucleation in a more narrow region as compared to the blunt crack, where creep strain accumulates rather uniformly around the circular crack notch (see Figure 5).

6. Effect of grain boundary sliding on cavitation

Experimental observations of creep tests show that grain boundary cavitation develops predominantly on facets that are more or less transverse to the the maximum principal tensile stress direction (see e.g. Argon, 1982; Cocks and Ashby, 1982). Therefore, most theoretical models have been developed for cavitation on transverse facets. For most of the lifetime, sliding rates on such facets are negligible. However, final intergranular fracture occurs when transverse microcracks link-up by either the sliding-off (low grain boundary viscosity) or failure (high viscosity) of inclined facets. In the present study, as well as in previous related studies (Van der Giessen and Tvergaard, 1994; Onck and Van der Giessen, 1997), the constitutive equations for cavitation do not incorporate a dependence on the grain boundary shear stress. Thus, these models may overestimate the time spent in the linking-up process (Chen, 1983a). Moreover, the creep crack growth calculations presented in the previous sections suggest that the linking-up of microcracks does often not occur in a direction where microcracks form first (see e.g. Figure 7). In this section we investigate how grain boundary sliding affects the linking-up process by incorporating the effect of shear stress into the cavity growth and nucleation relations. Due to the absence of proper micromechanical models, this will be done in an approximate manner.

The expression for the volumetric growth rate, given in (3), has been derived for a non-sliding facet. However, a sliding displacement as depicted in Figure 16(a) in combination with diffusional growth can give rise to non-equilibrium void shapes, as shown in Figure 16(b). Such void shapes have been observed experimentally by Chen and Argon (1981) and according to Chen (1983a) this is expected to have an important contribution to void growth in the final stages of creep life. Chen (1983b) introduced a quantitative model of diffusional cavity growth on sliding grain boundaries, but an expression for the volumetric growth rate

cannot easily be deduced from this study. Therefore, we account for the effect of sliding on cavity growth in a approximate manner. It is assumed that surface diffusion is so fast compared to sliding that the equilibrium shape is restored; the effect of sliding then is to have enlarged the cavity size. An upper bound to this effect is obtained by assuming that any sliding displacement, $|\Delta u_s|$, directly increases the void radius to $a + \frac{1}{2}|\Delta u_s|$, as illustrated in Figure 16(c). This yields an additional contribution of sliding rate to the volumetric growth rate of

$$\dot{V}_{\text{slid}} = 2\pi a^2 h(\psi) |\dot{u}_s|. \quad (15)$$

The value of $|\dot{u}_s|$ can be subsequently related to the grain boundary shear stress $|\tau|$ through (11), so that the total volumetric cavity growth rate can be written in the functional form

$$\dot{V} = \dot{V}_{\text{diff}}(\sigma_n) + \dot{V}_{\text{creep}}(\sigma_m, \sigma_e) + \dot{V}_{\text{slid}}(\tau), \quad (16)$$

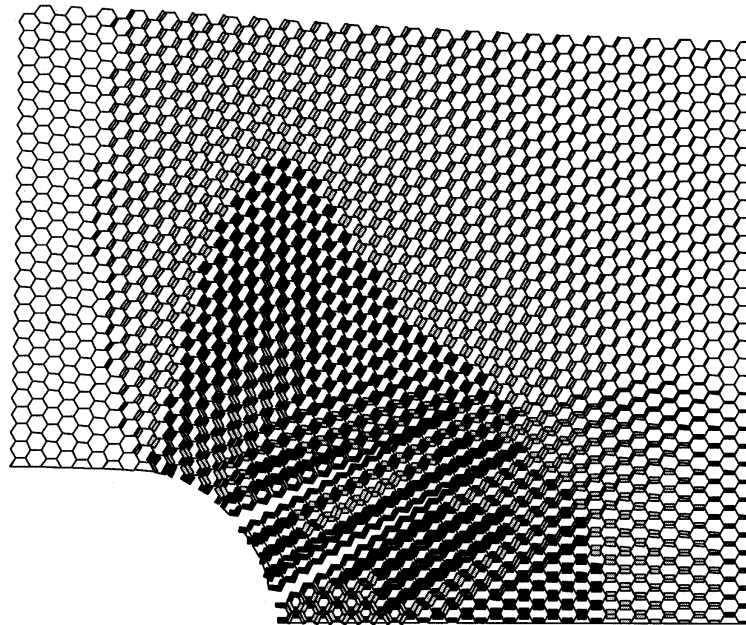
where only the stress dependencies are included.

As mentioned in Section 2, the continuous nucleation of grain boundary cavities is often associated with a stress concentration mechanism that acts throughout creep life in proportion to strain. So far, we have motivated our nucleation model from the notion that these stress concentrations result from the interaction of dislocations or slip lines with grain boundaries, causing small decohesions that can become stable cavities when the grain boundary is under a tensile normal stress. On the other hand, Argon and co-workers (e.g. Argon et al., 1980; Hsia et al., 1991) have argued that cavity nucleation is triggered by stress concentrations at irregularities such as second-phase particles on sliding grain boundaries. A simplistic, phenomenological manner to incorporate this as an additional contribution to the creep rate is to expand the nucleation law to become

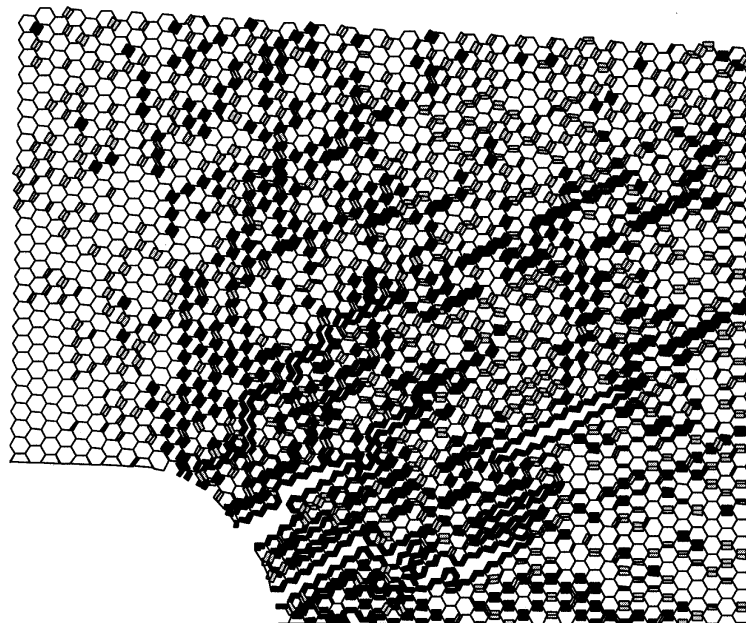
$$\dot{N} = F_n \left(\frac{\sigma_n}{\Sigma_0} \right)^2 (\dot{\epsilon}_e^C + \beta \dot{\epsilon}^{\text{sl}}), \quad \text{for } \sigma_n > 0, \quad (17)$$

with the sliding strain rate $\dot{\epsilon}^{\text{sl}}$ being defined as $\dot{\epsilon}^{\text{sl}} = |\dot{u}_s|/(2R_I)$ and β a parameter that expresses the material's sensitivity to shear-driven nucleation. As before, the sliding velocity \dot{u}_s is related to the grain boundary shear stress according to (11). For $\beta = 0$ we recover the nucleation law (9), used in the previous sections.

First, we analyze the effect of grain boundary sliding on cavity growth by adopting the parameters of the ductile case, as shown in Figure 7, but using (16) instead of (3). The initial stages of damage development are identical to the reference ductile case, until the moment corresponding to Figure 7(a). Then, in the regions where microcracking has occurred, shear stresses on -30° facets connecting the microcracks increase considerably, and this leads to accelerated cavity growth due to the shear contribution \dot{V}_{slid} . Figure 17(a) shows the cavitation state at $t/t_R = 2.14$ which is roughly at the same time as Figure 7(b). Comparison of the two reveals that the region in which both the horizontal and -30° facets are heavily cavitated is much more pronounced and that two dominant cracks have formed, which initiated in the early microcracked regions as shown in Figure 7(a). Next, we analyze the same case, but with a random distribution of the nucleation activity F_n , similar to that in Figure 11. Figure 17(b) shows the cavitation state at $t/t_R = 2.41$, which looks rather similar to the reference case without shear dependence, Figure 11(b), except that more damage is concentrated in front of the notch and that the crack grows at a slightly smaller angle.



(a)



(b)

Figure 17. Grain boundary cavitation state with shear-driven cavity growth according to (16), for $L_R/R_I = 0.032$.
(a) Uniform distribution of F_n , $t/t_R = 2.14$; (b) Random distribution of F_n , $t/t_R = 2.41$.

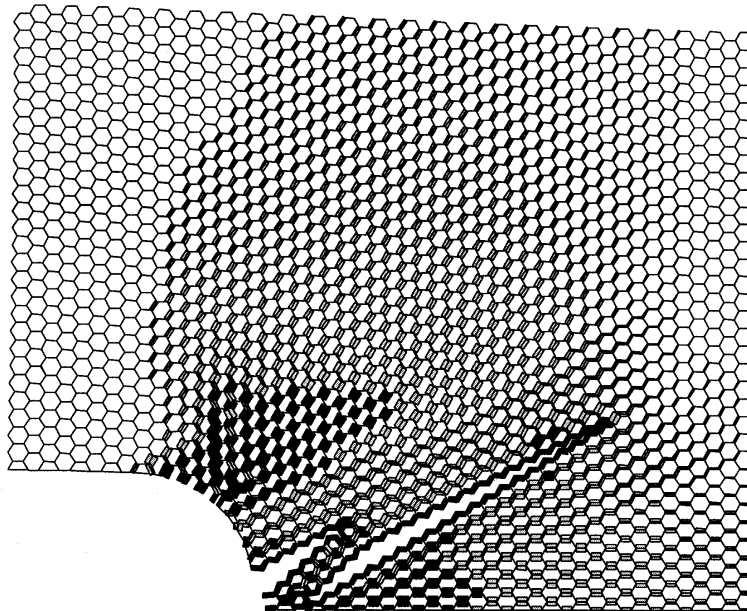
Next, we investigate the effect of shear stress on nucleation by again adopting the parameters of the ductile case, but using the shear-modified nucleation law (17), taking $\beta = 10$. Although damage on facets between microcracks develops more quickly, the crack growth pattern is similar to Figure 7. Using larger values of β did not significantly change this pattern. The underlying reason is that the initial stages of nucleation are dominated by the accumulation of creep strain, so that $\dot{\epsilon}_e^C \gg \beta \dot{\epsilon}^{sl}$ in (17). It is only once microcracking starts, that the shear stresses on inclined facets increase, resulting in a profound contribution of $\dot{\epsilon}^{sl}$ to the total nucleation rate. However, at that moment, cavity nucleation has almost saturated on most facets ($N = N_{\max}$), so that very few additional cavities can still be nucleated by grain boundary shearing.

To elucidate this further, we simply increase the maximum cavity density at which saturation takes place from $N_{\max} = 100N_R$ to $N_{\max} = 400N_R$. Doing so for the reference ductile calculation (Figure 7) but leaving $\beta = 0$ showed similar results as in Figure 7: coalescence at $a/b = 0.7$ still occurred at a cavity density of $N \approx 100N_R$, so that the maximum value N_{\max} was not attained. The ductile case using (17) with $\beta = 10$ and $N_{\max} = 400N_R$ (see Figure 18(a)) does lead to a relatively high cavity density at coalescence ($a/b = 0.7$): $N = N_{\max} = 400N_R$. Still, the initial stages of nucleation are dominated by creep deformation, until first microcracks develop. Then, however, stresses are redistributed to -30° facets, resulting in a considerable shear stress and accelerated, shear-driven nucleation. The propagation of the dominant, singular crack along the 30° direction in Figure 18(a) is mainly driven by nucleation, resulting from the high shear stresses on these facets.

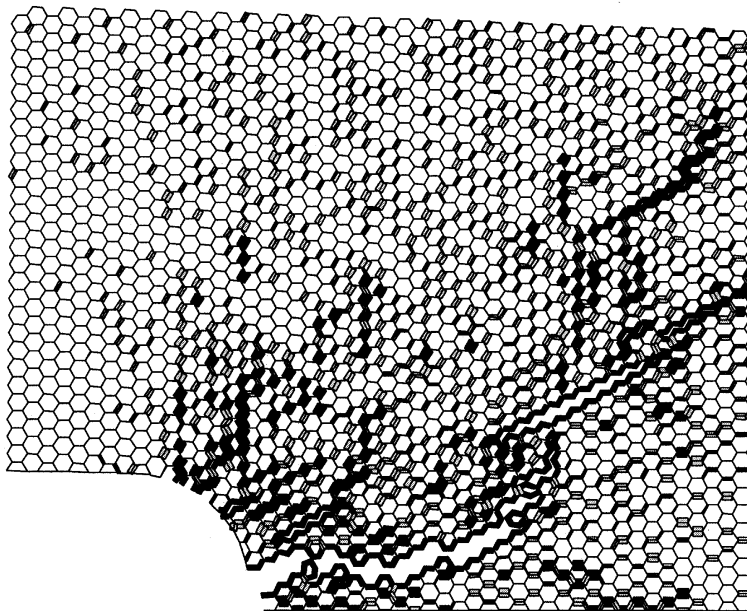
Finally, we analyze the same case, but investigate how random nucleation affects crack growth. Figure 18(b) corresponds to Figure 18(a), but with a random distribution of F_n , similar to Figure 11. Recall that a direct comparison with Figure 11 is relevant even though $N_{\max} = 100N_R$ there, since the calculation corresponding to Figure 11 with $N_{\max} = 400N_R$ showed similar results. We now see in Figure 18(b) that damage is much more localized and that one dominant crack forms, whose path is determined by the actual distribution of the nucleation activity F_n . Also note from the times at which Figs. 11(b) and 18(b) are taken, that the crack growth velocity is considerably increased by the additional contribution of shear to nucleation. However, no attempt is made to quantify this effect.

7. Discussion

Numerical simulations have been performed using a microstructural model which fully accounts for the discrete nature of intergranular creep crack growth. It has been found that blunting tends to shift the initial crack growth direction from $50^\circ - 60^\circ$ with the initial crack front for the sharp crack (see Figure 4) to approximately 30° for the blunt crack (Figures 7 and 8). The origin of the shift was related to the difference in initial stress and strain rate distributions for the two crack tip geometries. Straining and cavity nucleation for the sharp crack concentrates in a small region above the crack tip, and shifts to a more diffuse region in front of the tip for the blunt crack. Subsequent crack growth for both the sharp and blunt crack occurs in a direction where the facet normal stress distribution – the driving force for diffusional cavity growth – is favourable for linking-up (see Figs. 3 and 6). These observations were found to be persistent for both uniform and random distributions of the nucleation activity in the material and for both creep constrained (the ‘brittle’ case, $L_R/R_I = 0.1$) as well as unconstrained (the ‘ductile’ case, $L_R/R_I = 0.032$) cavitation.



(a)



(b)

Figure 18. Grain boundary cavitation state with shear-driven cavity nucleation according to (17) with $\beta = 10$ and $N_{\max} = 400N_R$, for $L_R/R_I = 0.032$. (a) Uniform distribution of F_n , $t/t_R = 1.44$; (b) Random distribution of F_n , $t/t_R = 1.37$.

At the macroscopic level, cavitation damage is often modelled in a smeared-out, average sense through continuum damage techniques. Two approaches can be identified: phenomenological damage equations, which are directly fitted to experiments (e.g. Hayhurst et al., 1984), or micromechanism-based continuum damage relations, based on a dilute distribution of cavitating grain boundary facets (e.g. Tvergaard, 1986; Li et al., 1988; Hsia et al., 1991). Both approaches have been demonstrated to be successful in predicting different crack growth behaviour as a function of material parameters and initial crack tip geometry. However, the origins of the various constitutive responses to multiaxial stress states are quite different. In the phenomenological approach, damage evolution is driven by a combination of effective stress and principal stress (but no reference is made to the underlying physical mechanisms), while in the micromechanism-based models damage evolution is mainly strain-controlled. In the latter, the strain dependence is a result of creep constrained cavitation on isolated facets for low stresses or of strain-driven, unconstrained cavity growth for higher stresses. It is interesting to note that in the present microstructural model the strain dependence only stems from strain-driven nucleation, and that the actual crack growth characteristics are determined by the mechanics related to the linking-up process. However, for the creep constrained conditions in the brittle case ($L_R/R_I = 0.1$), the severe stress-redistributions away from the crack tip gave the crack growth process a more stress-driven instead of strain-controlled appearance.

One of the persistent predictions of the present model is that crack extension has the tendency to move away from the median plane, even for a blunt crack where creep strain as well as principal stress concentrates in the symmetry plane. This tendency may be explained as representing the initial stages of meandering crack growth behaviour, which is often observed in experiments (see e.g. Hayhurst et al. 1984; Ozmat et al., 1991). However, in the numerical model symmetry conditions are imposed, so that zig-zag behaviour of one dominant crack around the symmetry plane is not possible. To remedy this, future work will focus on modelling the full unsymmetric problem, so that a meandering crack growth can be picked-up.

An essential ingredient of meandering behaviour is the linking-up process. Therefore, in Section 6 we investigated the effect of grain boundary sliding on both cavity growth and nucleation, which is expected to be important in the linking-up stages of creep crack growth. It was found for the ductile case ($L_R/R_I = 0.032$) that the effect on cavity growth was rather small, but that shear-driven nucleation has an accelerating effect on the linking-up process and favours the development of a single dominant crack. In view of this and the limited physical background of the nucleation law used so far (Onck and Van der Giessen, 1998a,b), there is ample room for improvement of the model for cavity nucleation.

The imposed symmetry and the uncertainties in the nucleation model mentioned above, preclude any definitive comparisons of the results obtained with the present type of modelling with experiments on creep crack propagation in real materials at this point. Yet, there are more of these idealizations that need to be further explored. Among these is the representation of the material by identical hexagonal grains, which corresponds to only three families of equal-sized facets, while a real material consists of a random distribution of facet sizes and orientations. To gain some insight into the effect of facet orientation, several calculations have been repeated for a 90°-rotated microstructure. In addition to the few results for freely sliding grains (see Section 5.2), more extensive comparisons have been presented in (Onck and Van der Giessen, 1998b) for the main cases studied here of viscous grain boundary sliding. These studies have demonstrated almost no effect on crack growth rate of microstructure and a mild one on crack

growth direction. Nevertheless, the statistical effects of the shape, size and orientation of real grains near cracks require further investigation.

A second noteworthy difficulty in a comparison between theory and experiment is the limited accuracy with which some of the parameters can be determined experimentally. This holds in particular for the grain boundary diffusion parameter \mathcal{D} , while the simulations have shown that the results are rather sensitive to its value through L_R .

Finally it must be noted that the present microstructural model is based on a planar representation of the polycrystalline aggregate, comprising regular hexagonal grains. Clearly, a real polycrystalline material corresponds to a 3-D spatial packing of randomly shaped grains. The integrity of such a 3-D packing is much higher than in 2-D (Anderson and Rice, 1985), which, for creep constrained conditions, leads to an out-of-plane constraint imposed by the staggered geometry of 3-D grains. This is obviously neglected in a 2-D analysis, which will therefore tend to overestimate the crack growth rates.

One may ask if it is possible to identify some of the parameter values in the model or to choose the proper nucleation model by confronting the predictions with experimental results. It appears, however, that the compound uncertainty of the aspects mentioned above precludes this at this stage. Further work is necessary to improve the model and to explore the dominant trends in the predictions.

References

- Anderson, P.M. and Rice, J.R. (1985). Constrained creep cavitation of grain boundary facets. *Acta Metallurgica* **33**, 409–422.
- Argon, A.S. (1982). Mechanisms and mechanics of fracture in creeping alloys. *Recent Advances in Creep and Fracture of Engineering Materials and Structures* (Edited by B. Wilshire and D.R.J. Owen), Pineridge press, Swansea, 1–52.
- Argon, A.S., Chen, I.-W. and Lau, C.W. (1980). Intergranular cavitation in creep: theory and experiments. *Creep-Fatigue-Environment Interactions* (Edited by Pelloux, R.M. and Stoloff, N.S.), AIMI, New York, 46–83.
- Ashby, M.F. (1972). Boundary defects and atomistic aspects of boundary sliding and diffusional creep. *Surface Science* **31**, 498–542.
- Chen, I.-W. (1983a). Mechanisms of cavity growth in creep. *Scripta Metallurgica* **17**, 17–22.
- Chen, I.-W. (1983b). Cavity growth on a sliding grain boundary. *Metallurgical Transactions A* **14**, 2289–2293.
- Chen, I.-W. and Argon, A.S. (1981). Creep cavitation in 304 stainless steel. *Acta Metallurgica* **29**, 1321–1333.
- Cocks, A.C.F. and Ashby, M.F. (1982). On creep fracture by void growth. *Progress in Material Science* **27**, 189–244.
- Crossman, F.W. and Ashby, M.F. (1975). The non-uniform flow of polycrystals by grain boundary sliding accommodated by power-law creep. *Acta Metallurgica* **23**, 425–440.
- Don, J. and Majumdar, S. (1986). Creep cavitation and grain boundary structure in type 304 stainless steel. *Acta Metallurgica* **34**, 961–967.
- Dyson, B.F. (1976). Constraints on diffusional cavity growth rates. *Metal Science* **10**, 349–353.
- Dyson, B.F. (1983). Continuous cavity nucleation and creep fracture. *Scripta Metallurgica* **17**, 31–37.
- Dyson, B.F. and McLean, D. (1977). Creep of Nimonic 80A in torsion and tension. *Metal Science* **11**, 37–45.
- Ghahremani, F. (1980). Effect of grain boundary sliding on steady creep of polycrystals. *International Journal of Solids and Structures* **16**, 847–862.
- Hayhurst, D.R., Brown, P.R. and Morrison, C.J. (1984). The role of continuum damage in creep crack growth. *Philosophical Transactions of the Royal Society of London A* **311**, 131–158.
- Hayhurst, D.R., Dimmer, P.R. and Morrison, C.J. (1984). Development of continuum damage in the creep rupture of notched bars. *Philosophical Transactions of the Royal Society of London A* **311**, 103–129.
- Hsia, K.J., Argon, A.S. and Parks, D.M. (1991). Modeling of creep damage evolution around blunt notches and sharp cracks. *Mechanics of Materials* **11**, 19–42.

- Li, F.Z., Needleman, A. and Shih, C.F. (1988). Creep crack growth by grain boundary cavitation: crack tip fields and growth rates under transient conditions. *International Journal of Fracture* **38**, 241–273.
- Lim, L.C. (1987). Cavity nucleation at high temperatures involving pile-ups of grain boundary dislocations. *Acta Metallurgica* **35**, 1663–1673.
- Needham, N.G. and Gladham, T. (1986). Intergranular cavity damage and creep fracture of 1Cr-0.5Mo steels. *Materials Science and Technology* **2**, 368–373.
- Needleman, A. and Rice, J.R. (1980). Plastic creep flow effects in the diffusive cavitation of grain boundaries. *Acta Metallurgica* **28**, 1315–1332.
- Onck, P.R. and Van der Giessen, E. (1997). Microstructurally-based modelling of intergranular creep fracture using grain elements. *Mechanics of Materials* **26**, 109–126.
- Onck, P.R. and Van der Giessen, E. (1998a). Growth of an initially sharp crack by grain boundary cavitation. *Journal of the Mechanics and Physics of Solids* (in print).
- Onck, P.R. and Van der Giessen, E. (1998b). Micromechanics of creep fracture: Simulation of intergranular crack growth. *Computational Materials Science* (in print).
- Ozmat, B., Argon, A.S. and Parks, D.M. (1991). Growth modes of cracks in creeping Type 304 stainless steel. *Mechanics of Materials* **11**, 1–17.
- Raj, R. and Ashby, M.F. (1975). Intergranular fracture at elevated temperature. *Acta Metallurgica* **23**, 653–666.
- Riedel, H. (1987). *Fracture at High Temperatures*, Springer-Verlag, Berlin.
- Sham, T.-L. and Needleman, A. (1983). Effects of triaxial stressing on creep cavitation of grain boundaries. *Acta Metallurgica* **31**, 919–926.
- Shih, C.F. (1983). Tables of Hutchinson-Rice-Rosengren singular field quantities. Report MRL E-147, Materials Research Laboratory, Brown University, Providence.
- Tvergaard, V. (1984a). On the creep constrained diffusive cavitation of grain boundary facets. *Journal of the Mechanics and Physics of Solids* **32**, 373–393.
- Tvergaard, V. (1984b). Constitutive relations for creep in polycrystals with grain boundary cavitation. *Acta Metallurgica* **32**, 1977–1990.
- Tvergaard, V. (1986). Analysis of creep crack growth by grain boundary cavitation. *International Journal of Fracture* **31**, 183–209.
- Van der Giessen, E. and Tvergaard, V. (1990). On cavity nucleation effects at sliding grain boundaries in creeping polycrystals. *Creep and Fracture of Engineering Materials and Structures* (edited by Wilshire, B. and Evans, R.W.), Elsevier, Swansea, 169–178.
- Van der Giessen, E. and Tvergaard, V. (1994). Development of final creep failure in polycrystalline aggregates. *Acta Metallurgica et Materialia* **42**, 959–973.
- Wu, R. and Sandström, R. (1996). Strain dependence of creep cavity nucleation in low alloy and 12%Cr steels. *Materials Science and Technology* **12**, 405–415.